A&A 561, A45 (2014)
DOI: 10.1051/0004-6361/201322215

Astronomy & Astrophysics

Thermophysical properties of near-Earth asteroid (341843) 2008 EV_5 from WISE data⋆

V. Alí-Lagoa[1,2], L. Lionni[3], M. Delbo[4], B. Gundlach[5], J. Blum[5], and J. Licandro[1,2]

[1] Instituto de Astrofísica de Canarias (IAC), c/ Vía Láctea s/n, 38205 La Laguna, Tenerife, Spain
e-mail: vali@iac.es
[2] Departamento de Astrofísica, Universidad de La Laguna, 38206 La Laguna, Tenerife, Spain
[3] University Paris VII – Diderot, 5 rue Thomas Mann, 75013 Paris, France
[4] UNS-CNRS-Observatoire de la Côte d'Azur, BP 4229, 06304 Nice Cedex 4, France
[5] Institut für Geophysik und extraterrestrische Physik, Technische Universität Braunschweig, Mendelssohnstr. 3, 38106 Braunschweig, Germany

Received 5 July 2013 / Accepted 23 October 2013

ABSTRACT

Aims. We derive the thermal inertia of 2008 EV_5, the baseline target for the *Marco Polo-R* mission proposal, and infer information about the size of the particles on its surface.
Methods. Values of thermal inertia were obtained by fitting an asteroid thermophysical model to NASA's Wide-field Infrared Survey Explorer (WISE) infrared data. Grain size was derived from the constrained thermal inertia and a model of heat conductivity that accounts for different values of the packing fraction (a measure of the degree of compaction of the regolith particles).
Results. We obtain an effective diameter $D = 370 \pm 6$ m, geometric visible albedo $p_V = 0.13 \pm 0.05$ (assuming $H = 20.0 \pm 0.4$), and thermal inertia $\Gamma = 450 \pm 60$ J m^{-2} s$^{-1/2}$ K^{-1} at the 1σ level of significance for its retrograde spin-pole solution. The regolith particles radius is $r = 6.6^{+1.3}_{-1.3}$ mm for low degrees of compaction and $r = 12.5^{+2.7}_{-2.6}$ mm for the highest packing densities.

Key words. minor planets, asteroids: individual: (341843) 2008 EV5 – infrared: planetary systems – radiation mechanisms: thermal

1. Introduction

Potentially hazardous, near-Earth asteroid (341843) 2008 EV_5, hereafter EV_5, has been selected as the baseline target of the sample return mission *Marco Polo-R*, proposed to the European Space Agency with a launch window between 2020 and 2024[1]. Studying the nature of the surface of EV_5 is therefore important, because collecting samples to obtain unaltered material will require different technological approaches depending on whether the outer layer consists of bare rock, fine-grained, or coarse-grained regolith. Information about regolith grain size can be derived using the heat conductivity model of Gundlach & Blum (2013) given a value of the thermal inertia, which in turn can be constrained by fitting a thermophysical model (TPM) to infrared data (see, e.g., Spencer et al. 1989; Spencer 1990; Lagerros 1996). Previous thermophysical studies of other mission targets can be found in, e.g., Müller et al. (2005, 2011), Wolters et al. (2011), and Müller et al. (2012).

Deriving surface physical properties of EV_5 is interesting for other reasons, too. First, thermal inertia plays a key role in the Yarkovsky effect, a non-gravitational dynamical force that induces a gradual drift in the orbits of asteroids with sizes of the order of 40 km and smaller (Bottke et al. 2006). Accounting for this effect is essential for determining accurate orbits of these objects, especially those classified as potentially hazardous (see Delbó & Tanga 2009, and references therein). Second, it was a very strong radar target that produced a high-resolution shape model at its December 2008 Earth approach (Busch et al. 2011). Finally, because even though its visible-to-near-infrared spectrum suggests that EV_5 belongs to the C-complex (Reddy et al. 2012) and is thus rich in carbonaceous materials, its geometric albedo of 0.12 ± 0.04 – derived from a diameter of 400 ± 50 m measured from radar observations by Busch et al. (2011) – is slightly outside the limit of what has traditionally been considered primitive. This is also the case for (2) Pallas and the Pallas collisional family (see, for example, Alí-Lagoa et al. 2013).

In this work we apply an asteroid thermophysical model to fit EV_5's outstandingly large set of infrared data obtained by NASA's Wide-field Infrared Survey Explorer (WISE) to derive its thermal inertia and draw conclusions about the characteristic particle size of the regolith on its surface.

2. Data

A general introduction to WISE can be found in Wright et al. (2010) and references therein. The NEOWISE project enhanced the WISE data processing system to allow detection and archiving of solar system objects (for details, see Mainzer et al. 2011a). We obtain the data from the WISE All-Sky Single Exposure L1b Working Database, available via the IRSA/IPAC archive[2].

WISE used four broad-band filters with isophotal wavelengths at 3.4, 4.6, 12, and 22 μm, referred to as W1, W2, W3, and W4, respectively (Wright et al. 2010). As explained in Alí-Lagoa et al. (2013), we follow a combination of criteria

⋆ Table of observed fluxes is only available at the CDS via anonymous ftp to cdsarc.u-strasbg.fr (130.79.128.5) or via http://cdsarc.u-strasbg.fr/viz-bin/qcat?J/A+A/561/A45

[1] See https://www.oca.eu/MarcoPolo-R/index.html

[2] http://irsa.ipac.caltech.edu/Missions/wise.html

found in Mainzer et al. (2011b), Masiero et al. (2011), and Grav et al. (2012) to ensure the reliability of the data. We implement the correction to the red and blue calibrator discrepancy in W3 and W4, and we use a cone search radius of 0.3″ centred on the MPC ephemeris of the object in our queries. All artefact flags other than p, P, and 0 and quality flags other than A, B, and C[3] are rejected, and we require the modified Julian date to be within four seconds of the time specified by the MPC. We ensure that the data is not contaminated by inertial sources by removing those points that return a positive match from the WISE Source Catalog within 6″. Finally, all remaining observations in band W1 were rejected since they are fewer than 40% of the data in the band with the maximum number of detections, namely W3. These criteria give a total of 489 useful data points, 158 in W2, 190 in W3, and 141 in W4.

Between EV_5's first and last observations by WISE, taken in 2010 Jan. 25 and March 7, the asteroid heliocentric distance decreased slightly, from 1.043 AU to 1.028 AU, it drew closer to the Earth by ~0.06 AU, from $\Delta = 0.335$ AU to $\Delta = 0.273$ AU, and the phase angle increased from 71.5° to 75.3°.

3. Thermophysical modelling of EV_5

In this section we briefly describe the most relevant aspects of the thermophysical model (TPM) we employ. For more details, see Delbó et al. (2007), Delbó & Tanga (2009), and Mueller (2007). The technique consists of modelling the observed flux as a function of a given set of parameters and finding the set of parameter values, in our case thermal inertia, surface roughness, and a scale factor s for the asteroid shape, that minimise the χ^2; i.e.,

$$\chi^2 = \sum_i \frac{\left(s^2 F_i - f_i\right)^2}{\sigma_i^2}, \quad (1)$$

where i runs through all observations, $s^2 F_i$ is the model flux, f_i the measured flux, and σ_i its corresponding error. Here, F_i is the unscaled mesh's model flux, which depends on its shape and spin axis orientation as a function of the geometry of the observation – phase angle and heliocentric and geocentric distances – and the asteroid's albedo, thermal inertia, and macroscopic surface roughness, with the last three assumed to be constant in time and throughout the surface. We also assume that thermal inertia does not depend on the temperature. The factor s^2 is related to how we model the size of the object. Each vertex of mesh is characterised by a vector in a given reference frame whose modulus is expressed in some given units. By multiplying all these vectors' moduli by the same linear scale s, we are able to change the model's size, and this factor is left free to vary and adjusted to minimise the χ^2. But because the model flux depends on the object's area projected towards the observer, which depends on the square of this scaling factor, the model flux is $s^2 F_i$.

The shape of the asteroid is represented by a set of 512 triangular facets based on a detailed radar shape obtained by Busch et al. (2011). We also took the following physical properties as input for the model: rotation period $P = 3.725 \pm 0.001$ h (Galad et al. 2009), absolute magnitude $H = 20.0 \pm 0.4$ (taken from the Small-Body Database of the Jet Propulsion Laboratory and rounded up to have one significant figure on the errorbar), and the retrograde pole-orientation solution preferred by Busch et al. (2011), namely (180°, –84°) ±10°. Though they conclude that EV_5 rotates retrograde, we also modelled the prograde solution, and our analysis consistently favours the retrograde case (for more details, see Sect. 4.1).

In the absence of macroscopic surface roughness and zero thermal inertia, the temperature of each facet is a function of the incident solar radiation absorbed, which in turn depends on its albedo, the heliocentric distance, and the projection of its area onto a plane perpendicular to the direction towards the Sun. Surface roughness is modelled by adding a hemispherical crater of opening angle γ_c and crater surface density ρ_c to each facet, which is the ratio of the area of the craters to the area of the facets. Each crater is in turn divided into facets (typically ~40) in order to introduce the effects of multiple scattering, which increases the surface temperature relative to the single scattering case. Non-illuminated crater facets (shadowed) may be heated by reflected sunlight and/or emission from other crater facets, so they also contribute to the flux if they are visible to the observer. The effects of thermal conduction towards layers beneath the surface are accounted for by numerically integrating the one-dimensional heat-diffusion equation in each crater facet for a given value of thermal inertia. The net energy absorbed is re-emitted assuming the facets emit like grey bodies ($\epsilon = 0.9$). Our TPM does not account for shape-shadowing effects, but we expect these to be negligible. To qualitatively justify this, we calculated the number of facets n_b with potential blockers located ≥20° above their horizons. For the three shape models we used, namely the model introduced by Busch et al. (2011) with $n_f = 3996$ facets and the simplified models with $n_f = 1024$ and $n_f = 512$, we find that n_b/n_f is about 0.05, a very low percentage considering that having such potential blockers above the local horizon does not necessarily imply shadowing, since the Sun can still be in a direction where it is visible, and it would probably not be blocked simultaneously for all these facets. This conclusion can also be drawn from the small total view factor calculated for EV_5 by Rozitis & Green (2013), which is the mean fraction of sky subtended by other facets of the model for any given facet.

We thus calculated model fluxes for a wide range of preset values of thermal inertia, surface roughness, bolometric Bond albedo, and rotational phase φ_0, and adopted as the best solution the one with the minimum χ^2. Thermal inertia values run from $\Gamma = 0$ to 2500 J m^{-2} s$^{-1/2}$ K^{-1}, which are values typical of perfectly insulating material and basaltic rock (Jakosky 1986). Following the procedure of Mueller (2007), we used four preset combinations of (γ_c, ρ_c) to model surface roughness: no roughness (0°, 0), low roughness (45°, 0.5), medium roughness (68°, 0.8), and high roughness (90°, 0.9). Since the rotational phase at the time of WISE observations cannot be accurately predicted from the rotational phase determined at the time of the radar observations (an error of 0.001 h for a period of about 3.725 h gives an error on the rotational phase of about 230 °/year), we treated φ_0 as a free parameter that took on all values multiple of 10° between 0° and 360°. For more details, see Sect. 4.3 and Matter et al. (2011), Finally, the bolometric Bond albedo was varied from 0.01 to 0.10.

4. Results

In this section we present the best-fitting values of parameters, whereas in the following sections we provide a detailed account of our thermophysical analysis of EV_5's WISE data, including the discarded prograde rotational solution of EV_5, the effect of simplifying the shape model to the one we used with fewer facets, the relative minima found in χ^2-Γ space, and other

[3] Indicating signal-to-noise ratios $S/N > 10$, $3 > S/N > 10$, and $2 > S/N > 3$, respectively.

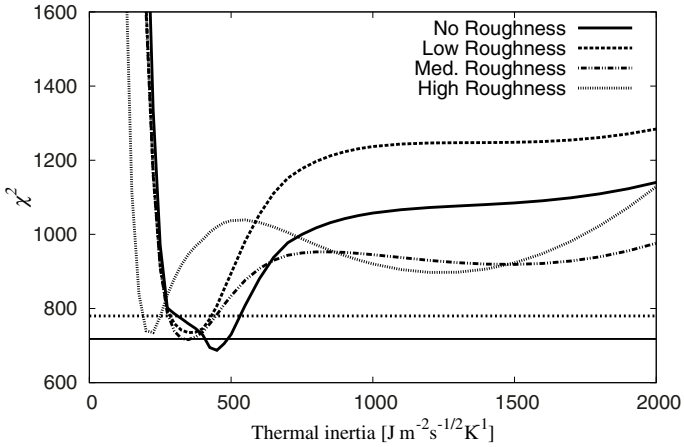

Fig. 1. χ^2 versus thermal inertia for the runs with $\varphi_0 = 130°$. The smooth surface case verifies the minimum χ^2 of all runs. The horizontal lines show the 1σ (black line) and 3σ (short-dashed line) levels at $\chi^2 = 718$ and $\chi^2 = 780$, respectively.

possible sources of error that may explain the slightly high minimum effective χ^2 achieved in our best-fit solution.

The minimum χ^2 corresponds to an effective diameter $D = 368.9$ m (the diameter of the sphere with the same volume as the scaled shape model), thermal inertia $\Gamma = 450$ J m^{-2} s$^{-1/2}$ K^{-1}, zero roughness ($\gamma_c = 0$, $\rho_c = 0$), Bond albedo 0.08, and rotational phase $\varphi_0 = 130°$ of the retrograde rotation model. In Fig. 1, we plot χ^2 vs. thermal inertia for the $\varphi_0 = 130°$ models. Interestingly, the χ^2 curve presents more than one relative minimum for some cases, a situation never reported before in the literature (for a more detailed discussion, see Sect. 4.2).

Our minimum $\chi^2 \approx 687$ is of the order of (though somewhat larger than) the effective number of degrees of freedom $\nu = N - n = 485$, where N is the number of data points, and $n = 4$ is the number of free parameters. Assuming that the data errors are normally distributed, our χ^2 statistic has a standard deviation of the order of $\sigma \sim \sqrt{2\nu} \simeq 31$ (see, for example, Press et al. 1986). To give a better idea of the goodness-of-fit and to estimate an errorbar for our best-fit parameters, we include the 1σ and 3σ levels in Fig. 1. Within a 1σ confidence level, we can constrain Γ to be within the interval (410, 490) J m^{-2} s$^{-1/2}$ K^{-1} and the surface roughness at a macroscopic level to be negligible, though the minimum χ^2 of the medium-roughness case is within the 1σ limit. On the other hand, at the 3σ level, we have $\Gamma \in (310, 530)$ J m^{-2} s$^{-1/2}$ K^{-1}, and it is not possible to constrain roughness. The effective diameter is $D = 370 \pm 20$ m at the 3σ level and $D = 368.9 \pm 0.5$ m at the 1σ level, which are within the errorbar of previous estimates. However, these errorbars do not take the propagation of the error in the spin-pole solution or the uncertainty in the Bond albedo into account, which we cannot constrain. Taking the conservatively broad range of values of Bond albedo, the 1σ errorbars in size and thermal inertia are increased: $D = 370 \pm 6$ m and $\Gamma = 450 \pm 60$ J m^{-2} s$^{-1/2}$ K^{-1}. The ensuing geometric visible albedo is $p_V = 0.13 \pm 0.05$, whose error is dominated by the uncertainty in the absolute magnitude. This value of p_V could be a small overestimate due to the systematic bias toward lower H-values (especially $H > 10$) of widely used catalogues detected by Pravec et al. (2012).

The situation with the rotational phase is more complicated. In Fig. 2, we show intensity maps of the χ^2 values as functions of thermal inertia and rotational phase for the different roughness cases separately. The white dashed lines show the 1σ and 3σ contours (when only one line is visible it corresponds to the latter case). At a 1σ level of significance, the zero-roughness case presents two broad intervals of φ_0-values with minimum χ^2, namely between 90° and 180°, and 300° and 330°. Again, we

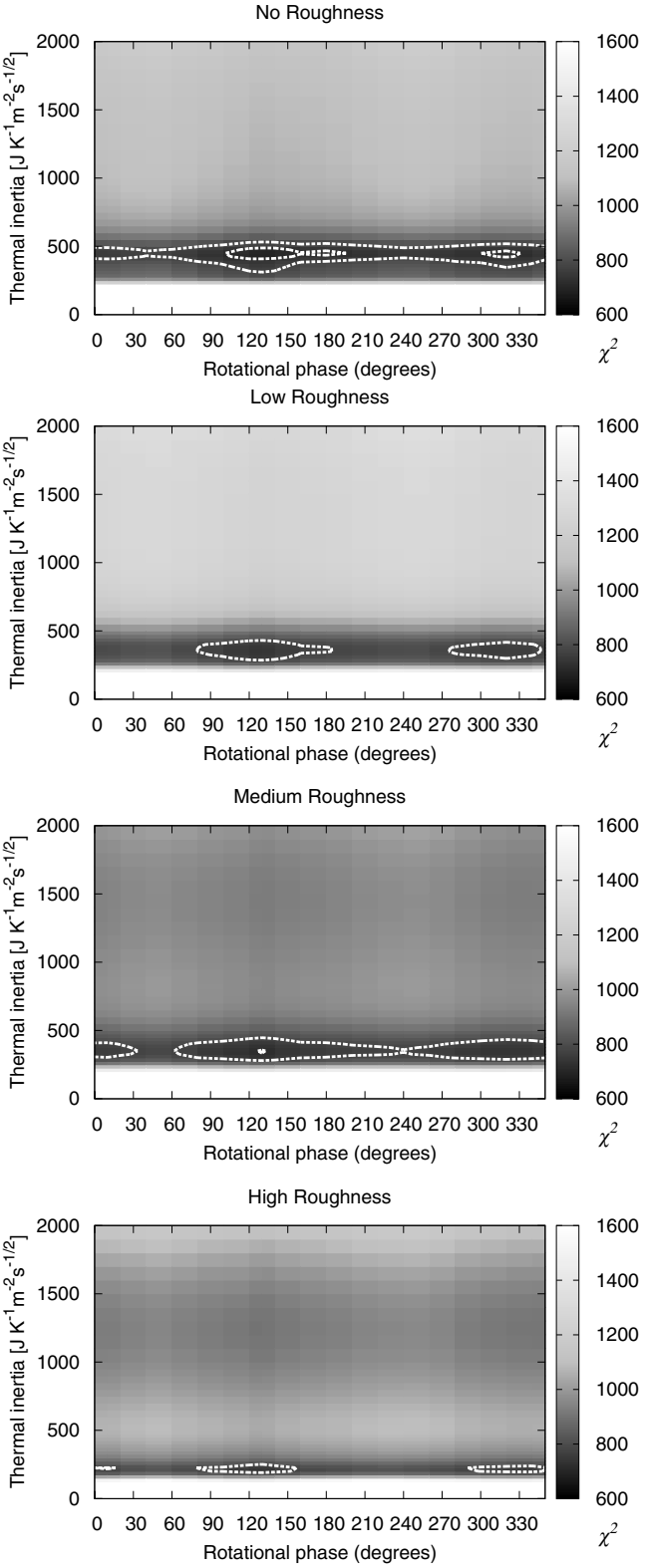

Fig. 2. Intensity map of χ^2 values in Γ-φ_0 space. The contour lines correspond to 1σ and 3σ values, the former only visible as the inner contours in the no-roughness and medium-roughness cases.

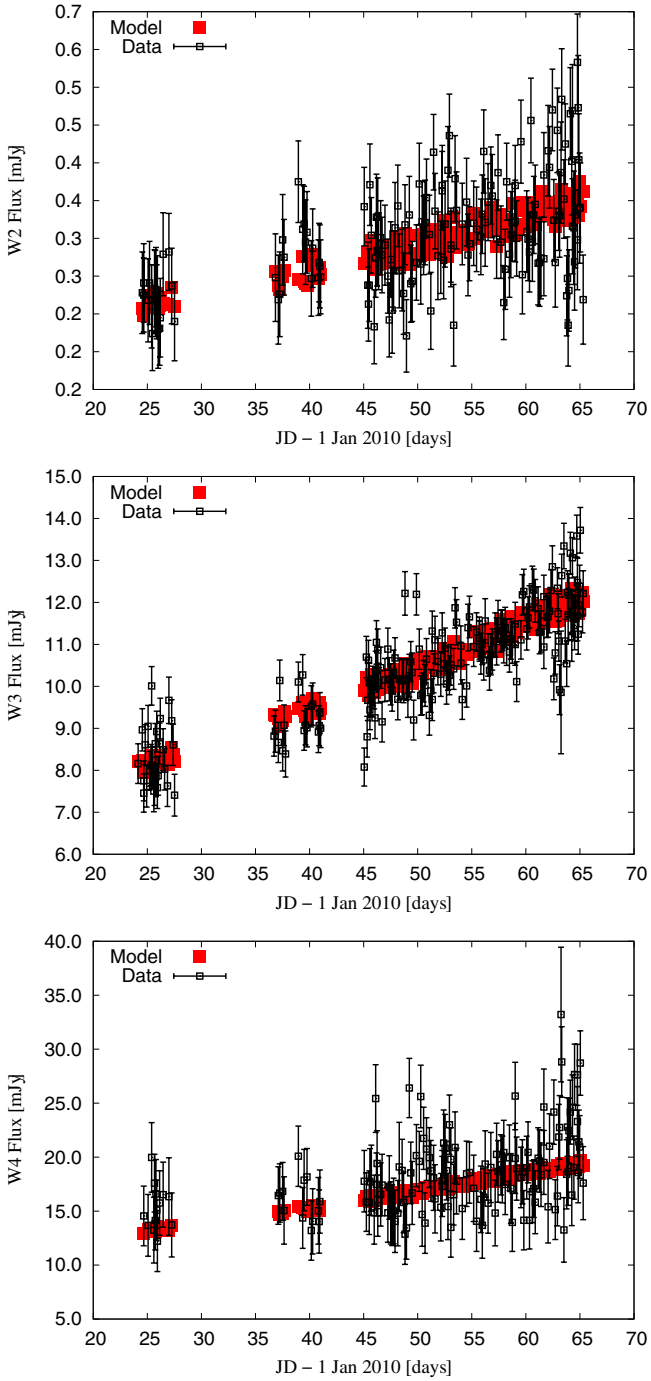

Fig. 3. WISE band fluxes (black empty squares) and corresponding thermophysical model values (red filled squares) plotted versus date for the complete data set. The rotational phase is 130° at epoch 2 455 221.534375, i.e., the Julian Date (JD) on 2010 January 25 00:49:29.6 UT.

cannot constrain φ_0 at the 3σ level. In these plots, one can also see additional shallower and broader minima at higher values of Γ for the medium- and high-rougness models.

In Fig. 3 we plot the observed and model fluxes versus Julian Date (hereafter JD, counting from 1 January 2010) for the model with the best-fitting parameter values. The data show a high degree of scatter as compared to the model, and visual inspection of these plots does not help choose among models with different but similar values of Γ or surface roughness since the data flux variations in the different bands mostly look uncorrelated to each other and the model. But while effects of shape, spin pole orientation, and rotational period are smaller than the data scatter, the thermal inertia and the diameter are well constrained by the TPM, which produces much better results for EV_5 than the near-Earth asteroid thermal model (NEATM, Harris 1998). NEATM considers a non-rotating, perfectly-diffusing (Lambertian), zero-thermal-inertia, spherical asteroid, whereas asteroids surfaces are almost always non-spherical, non-Lambertian, not exactly perfect insulators, and may be macroscopically rough. Thus, this idealised model uses a free parameter η, the so-called "infrared beaming parameter", which modifies its surface temperature distribution to fit the real thermal fluxes of asteroids better. The NEATM results reported for EV_5 in Table 1 of Masiero et al. (2011) cannot be directly compared because these authors do not fit the asteroid diameters when values are available from other more direct measurements (e.g., radar, stellar occultations), as is the case with EV_5's radar size from Busch et al. (2011). In addition, they use a different value of H than we use here, namely 19.7. From our NEATM, which essentially follows what is described by Mainzer et al. (2011b) and Masiero et al. (2011) and which we validated in Alí-Lagoa et al. (2013), we obtain higher but compatible values of infrared beaming parameter and size: $\eta = 2.2 \pm 0.4$ and 470 ±70 m.

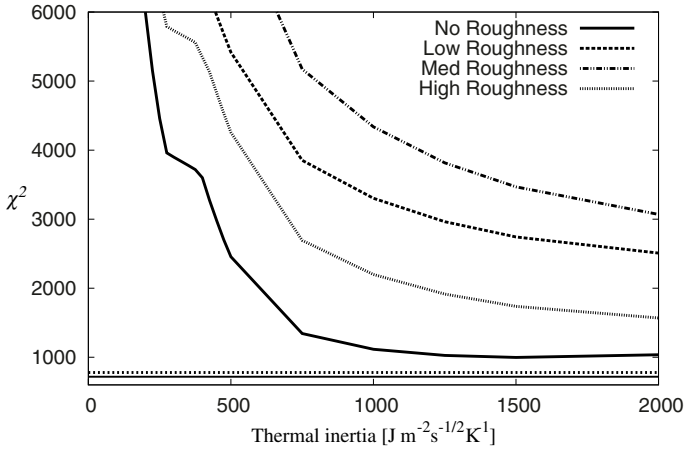

Fig. 4. χ^2 vs. thermal inertia for the prograde rotating model of EV_5 with four different values of surface roughness. The horizontal lines mark the value of the 1σ (continuous) and 3σ (short-dashed) levels of significance of the retrograde case (cf. Fig 1).

4.1. The prograde pole solution

We modelled the two spin solutions of EV_5 given by Busch et al. (2011). In Fig. 4 we plot the χ^2 vs. thermal inertia curves for the prograde case with four different values of roughness and rotational phase $\varphi_0 = 90°$, which verifies the minimum χ^2-values among all tested values of φ_0 (see Sect. 4). The minimum χ^2 for the prograde spin state clearly lies beyond the minimum values of the 1σ and 3σ levels of significance of the retrograde case. These results are expected since Busch et al. (2011) have already concluded that EV_5 rotates retrograde, but they quickly illustrate how thermophysical modelling can help distinguish between the two possible spin state solutions and at the same time confirm the radar results.

4.2. The effects of using a model with a reduced number of facets

The shape model we used resulted from the smoothing of the original shape model given by Busch et al. (2011); i.e., it is a

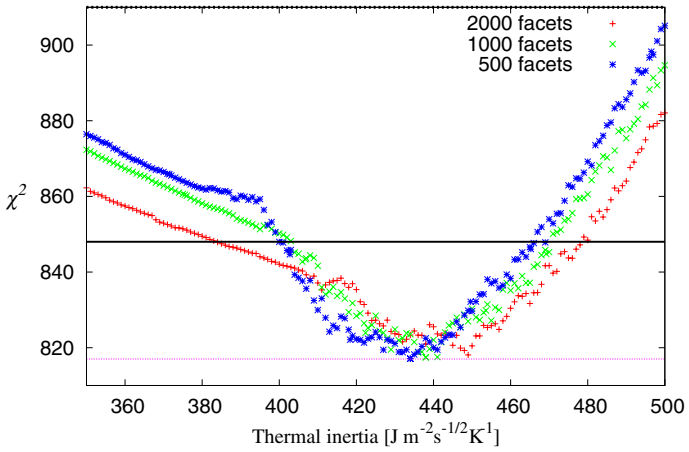

Fig. 5. χ^2 vs. thermal inertia for three shape models with varying number of triangular facets. The pink dashed horizontal line marks the minimum value of the χ^2 in the figure, whereas the black continuous line marks the 3σ limit for this solution.

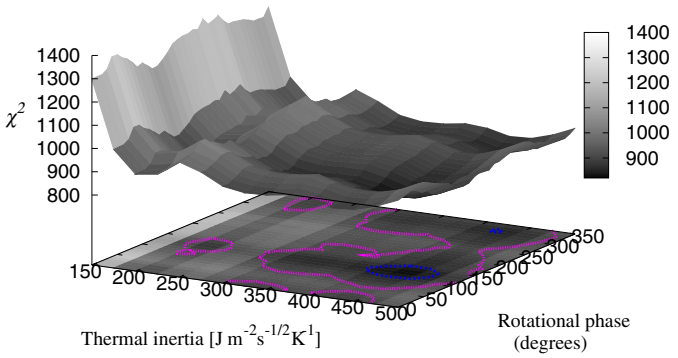

Fig. 6. Minimum χ^2 vs. thermal inertia vs. initial rotational phase. "Minimum χ^2" refers to the minimum among all four models with different surface roughnesses. The projection onto the $\Gamma-\varphi_0$ plane shows the 1σ (dark blue) and 3σ (pink) contours. The initial rotational phase that best fits the data is verified in the epoch 2010 January 25 00:49:29.6 UT.

recomputed triangular mesh with the desired smaller number of triangular facets. While this will clearly reduce the computing time, which is proportional to the number of facets, it may affect the best-fit values and introduce errors in the solution. To study the effects of this approximation, we carried out a sweep of thermal inertia values with a much narrower sampling step around the minimum for three shape models with different number of facets. In all three cases the best-fit solutions had $\varphi_0 = 130°$ and zero roughness. As shown in Fig. 5, where we plotted χ^2 vs. thermal inertia for those models, the shift in the best-fit value of Γ produced by this simplification is small compared with its estimated uncertainty. It is worth noting that the data set we used for this test is a preliminary one in which potential contamination by inertial sources was not addressed. In principle, very few non-inertial sources are expected to contribute significantly to the purely thermal bands W3 and W4, and in the particular case of EV_5, the thermal emission in W2 is also expected to dominate (see Sect. 4.4 below). Indeed, none of our conclusions would be changed if we had not removed possible contamination from inertial sources, though the χ^2 is reduced and the statistics improve slightly.

On the other hand, these tests showed a puzzling feature: there are several relative minima in the χ^2 curves of Fig. 5. These features are unexpected since, in accordance with the long-proven validity of the model, the χ^2 usually experiences a rapid increase when the values of the parameters are inadequate, and indeed such relative minima have never been reported before (to the best knowledge of the authors). One possibility is that these *secondary* minima are caused by slightly different values of thermal inertia and/or roughness better fitting different subsets of data, since those two parameters affect the shape of the lightcurve. Nevertheless, the data scatter is so large that it would be impossible to make a meaningful analysis by visual inspection, as might be done with a much smaller data set.

In addition, as already pointed out (see Figs. 1 and 2), there are broad relative minima in $\chi^2-\Gamma-\varphi_0$ space for the non-zero roughness cases. These broad minima are narrower and deeper (in relative terms) as roughness increases, which may be due to a trade-off between thermal inertia and roughness: higher degrees of roughness will increase the surface temperatures, which may be partially compensated for by high values of thermal inertia. However, as we increase the roughness to very high values, the interval of thermal inertia values that may compensate for it is smaller and the minima are thus narrower.

4.3. Initial rotational phase as a free parameter

We need to give the asteroid shape model the right orientation in space as a function of time. This is accomplished by applying an appropriate sequence of rotations to all vertices of the model at every step, as described, e.g., by Kaasalainen et al. (2002). These rotations are needed to perform the orientation as well as to change from ecliptic coordinates in a reference frame centred on the asteroid to cartesian coordinates in a frame co-rotating with the asteroid. In particular, the orientation corresponding to the instantaneous rotational phase φ is given by rotating the co-rotating frame an angle φ about the z-axis, which is aligned with the spin axis of the asteroid, taken as input in ecliptic coordinates. Rotational phase at any given time t is simply

$$\varphi = \varphi_0 + 2\pi\frac{t - t_0}{P} \tag{2}$$

where φ_0 is the corresponding value at t_0. An alternative way to motivate the use of an offset rotational phase φ_0 as a free parameter is given by Matter et al. (2011). In essence, the error in the absolute rotational phase of an asteroid grows in time after the reference epoch at which its period is determined. From Eq. (3) of Matter et al. (2011), we obtain $\Delta_\varphi \gtrsim 50°$ for EV_5, which leads us to revise the value of this parameter.

The thermophysical model does not, however, give a constraint for rotational phase at the 3σ level, but shows two intervals of possible φ_0-values at the 1σ level. In Fig. 6 we plot, for all pairs Γ-φ_0, the value of the minimum χ^2 of all four models with zero, low, medium, and hig roughness for the data set with potential contamination from inertial sources. By showing the 1σ and 3σ countours in dark-blue and pink colours, this plot illustrates at a glance the uncertainty intervals in the thermal inertia and rotational phase values for any value of roughness.

4.4. The reflected sunlight component in W2 data

The TPM used here does not include the reflected sunlight component of fluxes in bands W1 and W2 (W3 and W4 fluxes are thermal-emission dominated). Though we rejected EV_5 W1 data based on the minimum detection rate requirement (see Sect. 2), we would not have used this band in our modelling since W1

is dominated by reflected sunlight. Using the NEATM solution with $D = 0.4$ km, $\eta = 2.0$, and $p_{\rm IR} = 0.10$, we estimate that about two thirds of the flux is reflected sunlight. On the other hand, this component may contribute ~3% to the total W2 flux of EV_5. Failing to account for this could slightly but noticeably bias our results since, assuming[4] that all W2 points have signal-to-noise ratios (S/N) of 10, and given that we use 158 W2 points in our analysis, we would achieve an error ~1% on the mean W2 flux. Nevertheless, the two-parameter (H, G) phase function widely used to estimate the reflected sunlight for a given observation geometry (Bowell et al. 1989) has an uncertainty of about 5% in the final model flux in the W2 band. Because the contribution of the reflected light component itself is comparable to this uncertainty, we decided not to include it in the model.

4.5. The large concavity in EV_5's shape model

Busch et al. (2011) report that shape models without a large concavity could not fit EV_5 radar data. Though the concavity is still clearly visible in the simplified mesh, this feature could potentially be a source of inaccuracies given our simplification of the shape model and the multiple reflections between facets within the concavity. If this effect was significant, we would expect the model fluxes to deviate periodically in accordance with the phases of the period in which the concavity is visible to the observer. To test this, in Fig. 7 we plotted $((F_i - f_i)/\sigma_i)^2$ vs. relative rotational phase, p_i, for each WISE filter. Here, F_i are the model fluxes and $f_i \pm \sigma_i$ are the data points and corresponding errors at epoch of observation, t_i. The relative rotational phase is calculated from the epoch of observation as follows:

$$p_i = \frac{t_i - t_0}{P} - \mathrm{floor}\left(\frac{t_i - t_0}{P}\right), \tag{3}$$

where P is the period and t_0 is the first epoch of observation in EV_5's data set, which is arbitrarily chosen here as phase zero. In view of Fig. 7, there seem to be no periodic maxima in the deviations of the model fluxes with respect to the data consistent throughout the three WISE bands, so the concavity's effect is either satisfactorily accounted for by the model, or more likely, its effects are smaller than the data fluctuations. In any case, this is consistent with the conclusions of Rozitis & Green (2013), namely that the multiple reflections between its concavity and ensuing thermal emission do not have any influence on their prediction of EV_5's Yarkovsky-O'Keefe-Radzievskii-Paddack (YORP) effect, therefore it would be unexpected to see an influence on its thermal emision.

5. Regolith grain size

Thermal inertia measurements can be used to determine the grain size of the surface regolith of EV_5 (Gundlach & Blum 2013). In the following, we explain our strategy for the grain size determination.

First, the thermal inertia Γ is used to derive the heat conductivity λ of the surface regolith from

$$\lambda = \frac{\Gamma^2}{\phi \rho c}, \tag{4}$$

assuming plausible values for the volume-filling factor ϕ, the mass density ρ, and the heat capacity c of the surface regolith. Since the packing density of the surface material is not known,

[4] The largest S/Ns of EV_5's W2 data are ~10, though most have lower values, so this would be an upper limit.

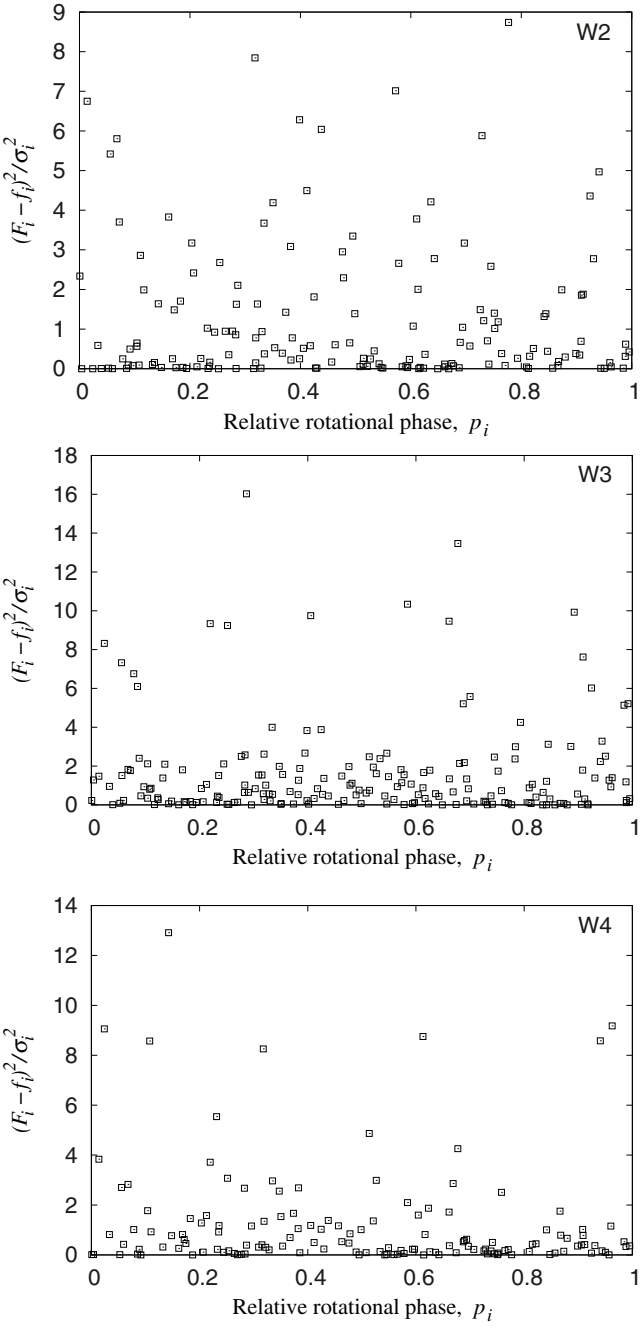

Fig. 7. Model-data deviations plotted against rotational phase for EV_5's data in bands W2, W3, and W4. The rotational phase is calculated from Eq. (3).

the volume filling factor ϕ is treated as a free parameter and is varied between $\phi = 0.1$ (extremely fluffy packing, plausible only for small regolith particles and low gravitational accelerations) and $\phi = 0.6$ (close to the densest packing of equal-sized particles) in steps of $\Delta\phi = 0.1$. For the density and the heat capacity of the surface material, laboratory measurements of the density and heat conductivity of representative meteorites for C-type asteroids (CM2-type Cold Bokkeveld and CK4-type NWA 5515) are used; i.e., $\rho = 3110\,\mathrm{kg\,m^{-3}}$ and $c = 560\,\mathrm{J\,kg^{-1}\,K^{-1}}$ (Opeil et al. 2010). Figure 8 shows the derived values of the heat conductivity, following Eq. (4), for the different volume filling factors of the material and for a thermal-inertia value of $450\,\mathrm{J\,m^{-2}\,s^{-1/2}\,K^{-1}}$.

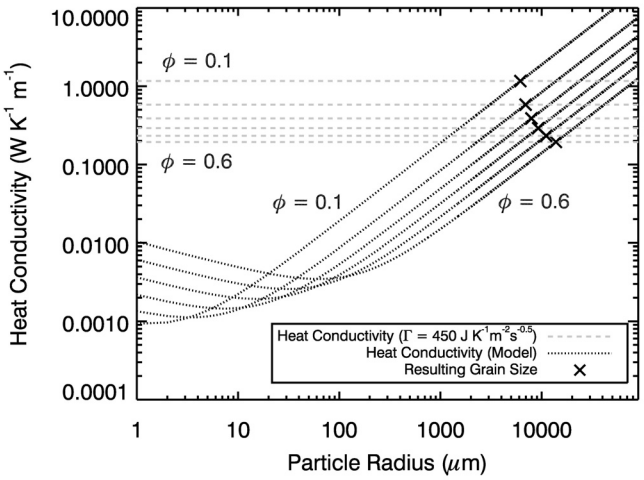

Fig. 8. Grain-size analysis for the surface regolith of EV_5. To estimate the mean grain size of the surface regolith, the heat conductivity of the surface material derived from the thermal inertia measurements (dashed lines) are compared with calculations of the heat conductivity of a model regolith (dotted curves) for six distinct volume-filling factors $\phi = 0.1, \ldots 0.6$.

To derive a typical regolith-grain size from the thermal-conductivity value, we calculate the heat conductivity of the surface material using a model for the heat conductivity of granular material in vacuum (for details, see Gundlach & Blum 2013), which gives

$$\lambda(r, T, \phi) = \lambda_{\rm solid}(T)\, H(r, T, \phi) + 8\,\sigma\,\epsilon\,T^3\,\Lambda(r, \phi). \quad (5)$$

Here, r and T are the mean regolith-grain radius and the regolith temperature, respectively. The first term on the right-hand side of Eq. (5) describes the heat conduction through the solid network of regolith particles. Here, $\lambda_{\rm solid}(T)$ is the heat conductivity of the bulk material of the regolith and $H(r, T, \phi)$ is the Hertz factor. The bulk heat conductivity of the surface material is derived from laboratory measurements of representative meteorites for C-type asteroids (Cold Bokkeveld and NWA 5515; see Opeil et al. 2010) by taking the porosities of the meteorites into account, $\lambda_{\rm solid} = (1.19 + 2.1 \times 10^{-3}\,T\,[\rm K])\,W\,m^{-1}\,K^{-1}$. The Hertz factor describes the reduced heat flux through the contacts between the regolith particles and depends on the mean radius of the regolith particles, on their temperature T and on the volume-filling factor of the surface material (for details, refer to Gundlach & Blum 2013). The Hertz factor also takes the irregularity of regolith-particle shapes into account and has been calibrated with lunar regolith (Gundlach & Blum 2013).

The second term in Eq. (5) takes the radiative heat conduction through the loose packing of regolith grains into account. Here, σ, ϵ, and $\Lambda(r, \phi)$ are the Stefan-Boltzmann constant, the emissivity of the regolith grains (assumed to be $\epsilon = 0.9$), and the mean free path of the photons within the pore space of the regolith. The mean free path of the photons within the regolith pore space depends on the volume-filling factor of the material and on the radius of the regolith grains and reads as $\Lambda = 1.34\frac{1-\phi}{\phi}r$ (see Gundlach & Blum 2013, for more details). The model predictions of the heat conductivity of the surface material, following Eq. (5), are shown in Fig. 8 for different volume-filling factors.

In the last step, the grain size of the surface regolith is derived from the comparison between the heat conductivity derived from the thermal-inertia measurements and the modelled heat conductivity as described above. One can see that the resulting grain radius, given by the intersections of the respective curves shown in Fig. 8, is generally smaller for lower volume filling-factors. For the low gravitational acceleration of EV_5 of $g = 7.5 \times 10^{-5}\,m\,s^{-2}$ (based on typical C-complex bulk densities of 1400 $kg\,m^{-3}$ given by Britt et al. 2002), it is possible that the inter-particle forces prevent the collapse of the regolith to its densest packing so that we cannot exclude low volume-filling factors of $\phi = 0.1, \ldots 0.2$. In this case, the mean particle radius is $r = 6.6^{+1.3}_{-1.3}$ mm. If, however, the inter-particle forces are negligible with respect to gravity, then packing densities of $\phi = 0.5, \ldots 0.6$ are expected so that the mean particle radius becomes $r = 12.5^{+2.7}_{-2.6}$ mm. The errors of the grain size estimations are then determined by quadratically adding the error of the thermal inertia measurements and the error due to the uncertainty in volume-filling factor. For the error of the thermal inertia measurements, we used the lower limit of $\Gamma = 410\,J\,m^2\,s^{-1/2}\,K^{-1}$ and an upper limit of $\Gamma = 490\,J\,m^2\,s^{-1/2}\,K^{-1}$.

6. Discussion

The thermal inertia of EV_5 obtained here is higher than the average value of km-sized NEAs ($200 \pm 40\,J\,m^{-2}\,s^{-1/2}\,K^{-1}$, Delbó et al. 2007), something to be expected for a smaller object. When compared to equally sized, S-type Itokawa ($750^{+50}_{-300}\,J\,m^{-2}\,s^{-1/2}\,K^{-1}$, Müller et al. 2005), EV_5's smaller thermal inertia may be explained by their different compositions (assuming similar degrees of porosity), since more primitive C-complex asteroid such as EV_5have much lower metallic content (or indeed none) than ollivine/pyroxene-rich S-types surfaces. When compared with other two similarly-sized, C-complex asteroids, (162 173) 1999 JU_3 and (175 706) 1996 FG_3, (for quick reference, see Table 3 of Gundlach & Blum 2013, and references therein), FG_3 is approximately a factor of 3 larger, and its thermal inertia is a third of EV_5's (Wolters et al. 2011), which results in its much smaller grain size of 0.03–0.2 mm. On the other hand, EV_5 and JU_3 have comparable gravitational acceleration and thermal inertia (Hasegawa et al. 2008) and their characteristic grain sizes are compatible within errorbars, though for EV_5 the maximum value is about a factor of 2 smaller. With its somewhat smaller grain size, EV_5's thermal inertia matching that of JU_3 could indicate a higher thermal conductivity and would be consistent with the suggestion of Busch et al. (2011) from radar albedo measurements – which are above the average for the 17 C-class, near-Earth asteroids observed with radar – that EV_5's surface material may contain some amount of metal. This can put a constraint on the possible meteorite analogues for EV_5. Reddy et al. (2012) studied visible-to-near-infrared spectra of EV_5 and preferred almost non-metallic, low-albedo CI chondrites based on spectral slope and an unconfirmed absorption band at 0.48 μm, but rejected as possible matches other carbonaceous chondrites (CR, CO, CH, and CK meteorites) with similar spectral slopes but higher metal content.

7. Conclusions

In this work we performed thermophysical modelling of WISE data of (341 843) 2008 EV_5 using the two spin-pole solutions given by Busch et al. (2011). Our results favour the retrograde case, consistent with the conclusions of Busch et al. (2011). The best-fit value of thermal inertia within 1σ; i.e., $\Gamma = 450 \pm 60\,J\,m^{-2}\,s^{-1/2}\,K^{-1}$, is attained for a rotational phase of $\varphi_0 = 130^{\circ+50^\circ}_{-30^\circ}$ and considering no surface macroscopic roughness, though the last two parameters are not constrained at a 3σ level of significance. The effective diameter and geometric visible

albedo are $D = 370 \pm 6$ m and $p_V = 0.13 \pm 0.05$, also consistent with previous determinations. The errorbar in D is at the 1σ level and does not take the uncertainty in the spin pole solution into account, so it is a minimum error estimate. From the mentioned value of Γ, the model of thermal conductivity by Gundlach & Blum (2013) results in a mean regolith-grain radius of $r = 6.6^{+1.3}_{-1.3}$ mm for low values of the volume-filling factor, and $r = 12.5^{+2.7}_{-2.6}$ mm for the highest packing densities.

Acknowledgements. We thank Dr. B. Rozitis for a thorough and constructive review that greatly improved this work. We have benefitted from discussions with J. Hanuš. V.A.L. acknowledges support from the project AYA2011-29489-C03-02 (MEC, former Spanish Ministry of Education and Science). This work was supported by the grant 11-BS56-008 (Shocks) of the Agence Nationale de la Recherche (ANR) of France. Bastian Gundlach was supported by D.F.G. under Grant Bl 298/19-1. J.L. acknowledges support from the projects AYA2011-29489-C03-02 and AYA2012-39115-C03-03 (MINECO, Spanish Ministry of Economy and Competitiveness). This publication uses data products from NEOWISE, a project of the Jet Propulsion Laboratory/California Institute of Technology, funded by the Planetary Science Division of the NASA. We made use of the NASA/IPAC Infrared Science Archive, which is operated by the Jet Propulsion Laboratory, California Institute of Technology, under contract with the NASA.

References

Alí-Lagoa, V., de León, J., Licandro, J., et al. 2013, A&A, 554, A71
Bottke, Jr., W. F., Vokrouhlický, D., Rubincam, D. P., & Nesvorný, D. 2006, Ann. Rev. Earth Planet. Sci., 34, 157
Bowell, E., Hapke, B., Domingue, D., et al. 1989, in Asteroids II, eds. R. P. Binzel, T. Gehrels, & M. S. Matthews (Tucson: University of Arizona Press), Proc. Conf., 524
Britt, D. T., Yeomans, D., Housen, K., & Consolmagno, G. 2002, in Asteroids III, eds. W. F. Boltkey Jr, A. Cellino, P. Paolicchi, & R. P. Binzel (Tucson: University of Arizona Press), 485
Busch, M. W., Ostro, S. J., Benner, L. A. M., et al. 2011, Icarus, 212, 649
Delbó, M., & Tanga, P. 2009, Planet. Space Sci., 57, 259
Delbó, M., Dell'Oro, A., Harris, A. W., Mottola, S., & Mueller, M. 2007, Icarus, 190, 236
Galad, A., Vilagi, J., Kornos, L., & Gajdos, S. 2009, Minor Planet Bull., 36, 116
Grav, T., Mainzer, A. K., Bauer, J., et al. 2012, ApJ, 744, 197
Gundlach, B., & Blum, J. 2013, Icarus, 223, 479
Harris, A. W. 1998, Icarus, 131, 291
Hasegawa, S., Müller, T. G., Kawakami, K., et al. 2008, PASJ, 60, 399
Jakosky, B. M. 1986, Icarus, 66, 117
Kaasalainen, M., Mottola, S., & Fulchignoni, M. 2002, in Asteroids III, eds. W. F. Boltkey Jr, A. Cellino, P. Paolicchi, & R. P. Binzel (Tucson: University of Arizona Press), 139
Lagerros, J. S. V. 1996, A&A, 310, 1011
Mainzer, A., Bauer, J., Grav, T., et al. 2011a, ApJ, 731, 53
Mainzer, A., Grav, T., Masiero, J., et al. 2011b, ApJ, 736, 100
Masiero, J. R., Mainzer, A. K., Grav, T., et al. 2011, ApJ, 741, 68
Matter, A., Delbo, M., Ligori, S., Crouzet, N., & Tanga, P. 2011, Icarus, 215, 47
Mueller, M. 2007, Doctoral Dissertation, Freie Universität Berlin, http://www.diss.fu-berlin.de/2007/471/indexe.html
Müller, T. G., Sekiguchi, T., Kaasalainen, M., Abe, M., & Hasegawa, S. 2005, A&A, 443, 347
Müller, T. G., Ďurech, J., Hasegawa, S., et al. 2011, A&A, 525, A145
Müller, T. G., O'Rourke, L., Barucci, A. M., et al. 2012, A&A, 548, A36
Opeil, C. P., Consolmagno, G. J., & Britt, D. T. 2010, Icarus, 208, 449
Pravec, P., Harris, A. W., Kušnirák, P., Galád, A., & Hornoch, K. 2012, Icarus, 221, 365
Press, W. H., Flannery, B. P., & Teukolsky, S. A. 1986, Numerical recipes (Cambridge: University Press)
Reddy, V., Corre, L. L., Hicks, M., et al. 2012, Icarus, 221, 678
Rozitis, B., & Green, S. F. 2013, MNRAS, 433, 603
Spencer, J. R. 1990, Icarus, 83, 27
Spencer, J. R., Lebofsky, L. A., & Sykes, M. V. 1989, Icarus, 78, 337
Wolters, S. D., Rozitis, B., Duddy, S. R., et al. 2011, MNRAS, 418, 1246
Wright, E. L., Eisenhardt, P. R. M., Mainzer, A. K., et al. 2010, AJ, 140, 1868